# Design of Ferroelectric Organic Molecular Crystals with Ultrahigh Polarization

Shuang Chen and Xiao Cheng Zeng*

Department of Chemistry and Nebraska Center for Materials and Nanoscience, University of Nebraska-Lincoln, Lincoln, Nebraska 68588, United States

Ⓢ Supporting Information

ABSTRACT: Inspired by recent successful synthesis of room-temperature ferroelectric supramolecular charge-transfer complexes, i.e., tetrathiafulvalene (TTF)- and pyromellitic diimide (PMDI)-based crystals (Tayi et al. *Nature* **2012**, *488*, 485−489), three new ferroelectric two-component organic molecular crystals are designed based on the TTF and PMDI motifs and an extensive polymorph search. To achieve energetically favorable packing structures for the crystals, a newly developed computational approach that combines polymorph predictor with density functional theory (DFT) geometry optimization

Theoretical Design of Hydrogen-Bonded arTTF-PMDI crystal with High Polarization of 127 μC/cm²

is employed. Tens of thousands of packing structures for the TTF- and PMDI-based crystals are first generated based on the limited number of asymmetric units in a unit cell as well as limited common symmetry groups for organocarbon crystals. Subsequent filtering of these packing structures by comparing with the reference structures yields dozens of promising crystal structures. Further DFT optimizations allow us to identify several highly stable packing structures that possess the space group of $P2_1$ as well as high to ultrahigh *spontaneous polarizations* (23−127 μC/cm²) along the crystallographic *b* axis. These values are either comparable to or much higher than the computed value (25 μC/cm²) or measured value (55 μC/cm²) for the state-of-the-art organic supramolecular systems. The high polarization arises from the ionic displacement. We further construct surface models to derive the electric-field-switched low-symmetry structures of new TTF- and PMDI-based crystals. By comparing the high-symmetry and low-symmetry crystal structures, we find that the ferroelectric polarization of the crystals is very sensitive to atomic positions, and a small molecular displacement may result in relatively high polarizations along the *a* and *c* axes, polarity reversal, and/or electronic contribution to polarization. If these newly designed TTF- and PMDI-based crystals with high polarizations are confirmed by experiments, the computer-aided ferroelectric material design on the basis of hydrogen-bonded charge-transfer complexes with flexible electron-donor and acceptor molecules would be proven valuable for expediting the search of room-temperature "displasive-type" ferroelectric organic crystals.
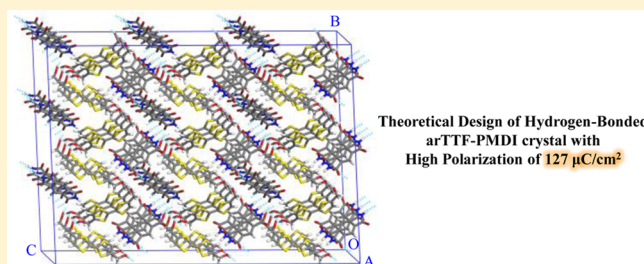
I. INTRODUCTION

Ferroelectricity, a property that enables switching electric polarization under the influence of an external electric field, has found wide applications in random access memories (RAMs), dynamic random access memory (DRAM) capacitors, field-effect transistors (FETs), electron emitters, and weak-magnetic field sensors.[1,2] Thus far, inorganic ferroelectric materials have been widely used for device application. In the ferroelectric process, the pyroelectric and piezoelectric effects prevail. To expand applications of ferroelectric materials to electro-optical and electromechanical processes, increasing attentions have been placed on light, flexible, and nontoxic organic ferroelectrics.

The first organic ferroelectric crystal, namely, the Rochelle salt (which contains organic tartrate ions), was discovered in 1921.[3] Over the past century, however, development of the organic ferroelectrics had been quite slow. Recently, a large number of organic ferroelectrics have been synthesized specially after the design strategies for achieving ferroelectricity were established.[4] One possible design is to incorporate components

with permanent dipoles such as thiourea[5] and vinylidene fluoride[6,7] into the organic solids so that the ferroelectric transition can arise from the orientation change of these polar components. Another possible design is to create spontaneous polarization, particularly in nonpolar organic materials, through relative displacement of ions in the organic crystals, especially for the charge-transfer (CT) complexes. As shown in Figure 1a, the CT complexes contain electron donor (ED) and acceptor (EA) layers that are stacked alternately along a particular direction. Electrons can transfer between the nonpolar donor−acceptor (DA) pairs along the stacking axis (measured in term of degree of charge transfer ρ). Electron transfer (measured in term of ρ') can be regenerated by external stimuli (either by an electric field or temperature) due to the change of stacking style of DA pairs (including the interlayer translation, slip, tilt, and rotation). Concomitant with this phase change (high-symmetry (HS) versus low-symmetry (LS) structures), the ferroelectric
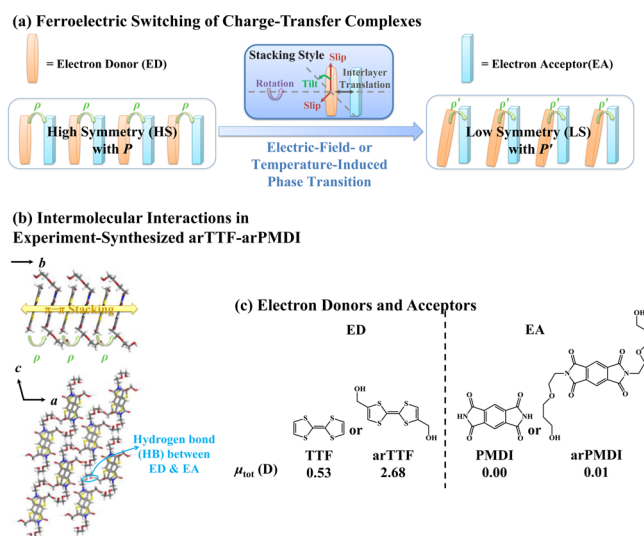
Figure 1. (a) Schematic representation of electric-field- or temperature-induced ferroelectric switching of charge-transfer complexes between different phases (HS versus LS phases). Upon the ferroelectric switching, the donor and acceptor molecules change their stacking style, resulting in ionic displacement and charge redistribution to finally produce different polarizations (P versus P'). (b) Description of weak intermolecular interactions such as $\pi-\pi$ stacking, charge transfer, and hydrogen bonding, involved in experimental arTTF-arPMDI crystals. (c) Electron donor and acceptor molecules considered in this study. The dipole moment (μ_{tot}) of each molecule is calculated at the level of B3LYP/6-31G(d), implemented in *Gaussian 09* software package.[19]

polarization of CT complex is switched (P versus P'). A series of widely studied CT complexes, i.e., the mixed-stack tetrathiafulvalene (TTF) and halogenated quinones such as chloranil (CA) and bromanil (BA), belong to this class of ferroelectric organic materials, and their ferroelectric switching is below 71 K.[8−10] These CT complexes can also undergo the temperature-induced neutral-to-ionic (NI) transition while altering the ferroelectric ordering.[8,11] Because most of these CT complexes are semiconducting, the NI transition requires a narrow charge gap which may lead to the electric leakage and degrade the spontaneous polarization.[4,11] One way to overcome this problem is to introduce additional hydrogen bonding into the two-component organic crystals. For example, Horiuchi et al. synthesized the hydrogen-bonded co-crystals of nonpolar phenazine (Phz) and chloranilic or bromanilic acids (H_2xa) to achieve very large spontaneous polarizations at room temperature.[12−14] Different from the mixed-stack TTF-CA and TTF-BA crystals, the Phz and H_2xa molecules form uniform π-stacking columns along the molecular b axis, and the hydroxyls of H_2xa donate protons to the N atoms of Phz in the lateral ($a-c$) dimensions.[12−14] The crystal is polarized along the b axis, and the underlying hydrogen bonds are the building bridges without having explicit proton transfer during the phase transition.[12−14] For the hydrogen-bonded cocrystal of H_2ca. and dimethyl-2,2′-bipyridine (55DMBP), the ferroelectric switching is attributed to the proton transfer.[4,14] The proton-transfer mechanism is also seen in single-component low-molecular-mass molecular crystals such as croconic acid, 2-phenylmalondialdehyde, 3-hydroxyphenalenone, or cyclobutene-1,2-dicarboxylic acid.[15,16] Through the keto−enol transformation, their molecular polarities are realigned by an external electric field to realize the spontaneous polarizations

($3-21$ $\mu C/cm^2$) at room temperature.[15,16] The benzimidazole series as the single-component molecular crystals are also investigated by Horiuchi et al. to show room-temperature ferroelectricity with appreciable polarizations ($5-10$ $\mu C/cm^2$) through proton tautomerization.[17] Three benzimidazole crystals even exhibit antiferroelectricity.[17]

As mentioned above, the hydrogen-bonded supramolecular networks generally possess the room-temperature ferroelectricity. In particular, the displacive-type ferroelectric materials can often give rise to large magnitude of spontaneous polarization. To incorporate all these advantageous features of organic ferroelectrics into a single material, Tayi et al. synthesized the hydrogen-bonded CT complexes based on TTF-based donor (named as arTTF) and pyromellitic diimide (PMDI)-based acceptor (named as arPMDI) to accomplish the room-temperature ferroelectric switching (see Figure 1b).[18] The ED and EA molecules have short hydroxymethyl and long diethylene glycol "arms", and these "arms" can act as proton donors and acceptors in the formation of hydrogen bonds.[18] Within this crystal, several weak intermolecular interactions are present including $\pi-\pi$ stacking, charge transfer, and hydrogen bonding. The room-temperature ferroelectricity likely stems from a complicated interplay between these interactions. In order to understand the significant contribution by conjugated core or hydrogen bonds from the functionalized "arms" toward the room-temperature ferroeletricity in the CT crystals, we construct three new two-component molecular crystals with both ED and EA molecules, namely, arTTF-PMDI, TTF-arPMDI, and TTF-PMDI by simply removing diethylene glycol "arms", hydroxymethyl "arms", or both "arms" in the experimental arTTF-arPMDI crystal (detailed discussion about the reference structures is given in Section S1 in the Supporting Information). The nonpolar electron donors and acceptors are present in Figure 1c with their dipole moments (calculated at the B3LYP/6-31G(d) level implemented in Gaussian 09 software package[19]). We find that all three new crystals possess high electric polarization ($27-51$ $\mu C/cm^2$; see Table S2). Thus, we can use them as reference structures or a guide for searching more stable ferroelectric crystals with even higher polarizations, because these more stable TTF- and PMDI-based crystals are likely to have quite different packing structures from the initially constructed structures.

To search for more stable crystals with high electric polarizations, we use the following strategies: First, we use a polymorph predictor implemented in Materials Studio 6.1 Polymorph module[20] to predict various crystal structures based on a Monte Carlo (MC) simulated annealing procedure. For each targeted crystal, typically, tens of thousands of packing structures are obtained. Next, by comparing with the reference crystal structures, dozens of packing structures are selected according to certain selection rules (see below) for further structural optimization using density-functional theory (DFT) methods implemented in the Vienna ab Initio Simulation Package (VASP 5.3).[21,22] More computational details on DFT calculations are given in Section S2 in the Supporting Information. Based on the DFT total-energy calculations, several low-energy crystal structures are obtained. Ferroelectric properties of these new crystals are investigated using the Berry phase method[23−25] as implemented in the VASP. Overall, three arTTF-PMDI, three TTF-arPMDI, and one TTF-PMDI low-energy crystals, all with high symmetry and high or even ultrahigh spontaneous polarizations ($23-127$ $\mu C/cm^2$), are predicted. Last, the origin of high polarization for these new
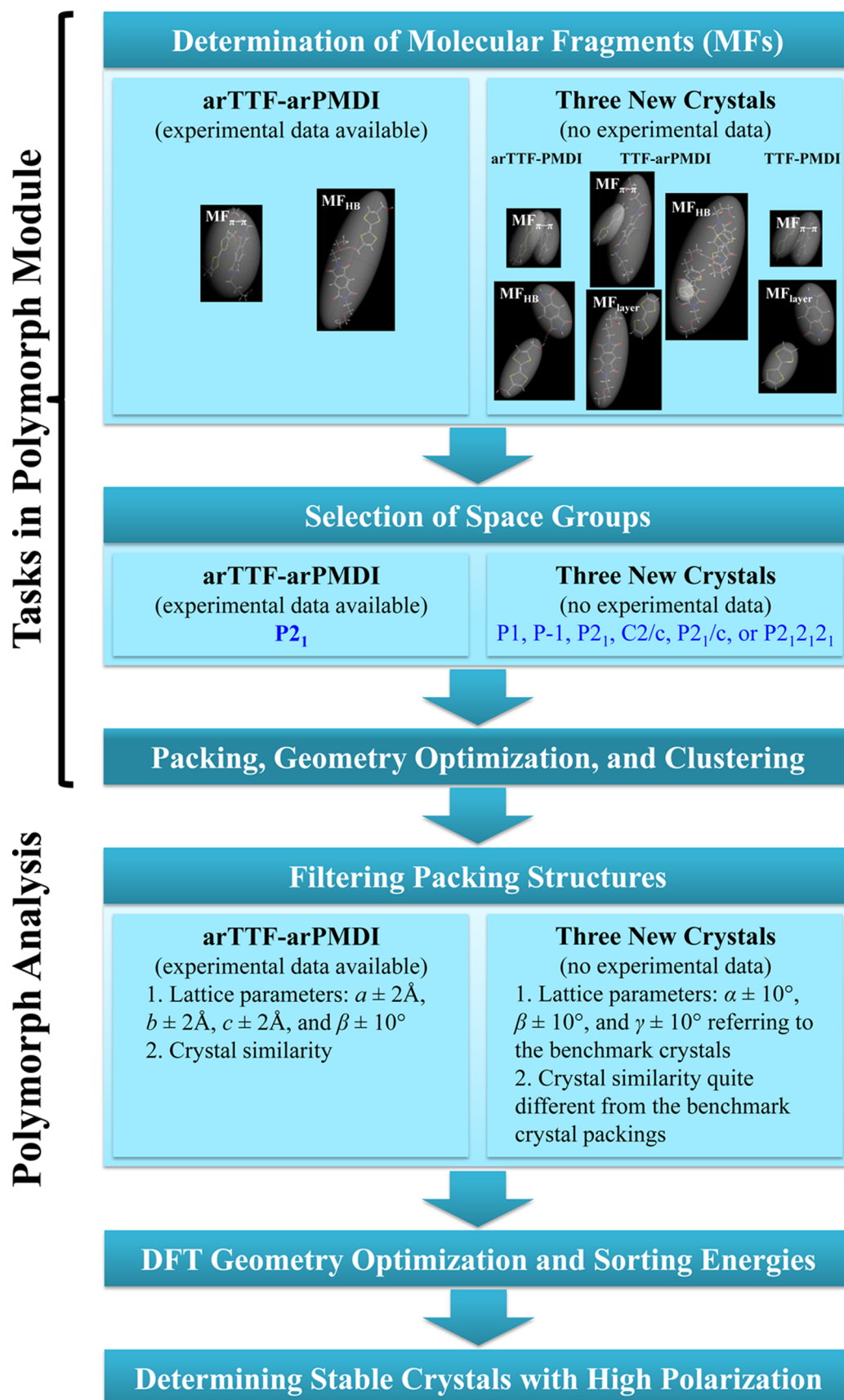
Figure 2. Schematic representation of crystal search steps for the experimental arTTF-arPMDI and new arTTF-PMDI, TTF-arPMDI, and TTF-PMDI crystals, respectively.

crystals is explored by implementing an electric-field-switched surface model (see Section S3 for more details). As a result, a low-symmetry (LS) structure for each new crystal is attained to compute their ferroelectric properties. To our knowledge, theoretical design of room-temperature ferroelectric two-component organic molecular crystals has not been reported in the literature.

II. CRYSTAL STRUCTURE PREDICTION

Taking Experimental Crystal as a Benchmark. Figure 2 illustrates a flowchart of the structure search steps. Here, we use the experimental arTTF-arPMDI crystal structure as a benchmark to examine the proposed crystal-structure search steps. First, we employ the Monte Carlo simulated annealing procedure implemented in the Polymorph module of Materials Studio 6.1[20] to collect a variety of packing arrangements for each crystal. The required inputs are predetermined molecular fragments (MFs) (see Figure 2) which can be treated as a rigid entity for the packing. Note that the experimental arTTF-arPMDI crystal entails three types of weak intermolecular interactions, including the $\pi-\pi$ stacking, charge transfer, and hydrogen bonding. A simple way to choose MFs is to take a DA pair along the mixed stacking column (see $MF_{\pi-\pi}$ in the top panel of Figure 2), in view of that the intrapair interactions include the $\pi-\pi$ stacking and charge transfer; and to take the otherDA pair (MF_{HB}) within the lateral ($a-c$) dimension, in which the intermolecular interaction between ED and EA is hydrogen bonding. Here, the COMPASS force field[26−28] is adopted to model the TTF- and PMDI-based crystal packing, and the detailed force-field parameters are given in Table S3. To validate the selection of the COMPASS force field, we compare binding energies between electron and proton donor and acceptor molecules for some typical packing conformers of both high- and low-symmetry arTTF-arPMDI crystals calculated from the COMPASS force field with those calculated from *ab initio* calculations (at the MP2/6-31G(d) level with including the basis set superposition error (BEES) correction[29,30]). Here, the COMPASS binding energies are computed using the Forcite module implemented in Materials Studio 6.1.[20] As shown in Table S4, qualitative agreements between the COMPASS and MP2 calculations can be concluded in view of the energy difference between the two levels of theory for the $\pi-\pi$ stacking conformers being less than 4.5 kcal/mol, and for the hydrogen binding conformers being less than 2.7 kcal/mol. We then use the polymorph predictor coupled with the COMPASS force field to generate a variety of crystalline packing structures based on the two MFs mentioned above, all under the constraint of the specific space group, $P2_1$, for the experimental arTTF-arPMDI crystal.

Subsequent to the crystalline packing structures generated through the MC simulated annealing procedure, geometry optimization and clustering steps in the Polymorph module are undertaken to further refine the packing structures. Here for all calculations in the Polymorph module, the computational quality is selected to be ultrafine, and the force-field-assigned charges are adopted. In addition, the electrostatics interactions are calculated using the Ewald summation method.[31] At this stage, by virtue of the Polymorph analysis, properties of thousands of generated packing structures are listed in a study table. Next, the crystal similarity of each packing structure can be analyzed by referring to the experimental arTTF-arPMDI crystal. Further narrowing down the range of lattice parameters ($a \pm 2$ Å, $b \pm 2$ Å, $c \pm 2$ Å, and $\beta \pm 10°$) with respect to the

experimental arTTF-arPMDI crystal, we can filter through a total of eight packing structures based on the Polymorph analysis. The eight potential packing structures are then subjected to the structural optimization using the DFT method. These optimized structures and corresponding energies are summarized in Table S5. The packing structure with the lowest energy (No. 7 in Table S5) is indeed very close to that of the optimized arTTF-arPMDI crystal at the DFT level. Their differences in lattice parameters are quite small (for a, b, and c < 0.07 Å and for β < 0.4°), and their energy difference is merely 0.8 meV per atom. In summary, our crystal-structure search procedure appears to be effective based on the benchmark test with the experimental crystal structure.

Determining Structures of New Stable Crystals. The prediction of more stable crystal structures for three new TTF- and PMDI-based crystals is less straightforward due to the lack of experimental data as a guide. Again, the crystal-search steps are illustrated in Figure 2 (right column). Note, however, that a crystal-structure search examining all possible MFs and space groups is impractical. To narrow down the scope of an open-ended search, a statistical analysis of the organic crystal structures recorded in the Cambridge Structural Database indicates that only about 8% of crystals have more than one formula unit in the asymmetric unit, and five space groups ($P-1$, $P2_1$, $P2_1/c$, $C2/c$, and $P2_12_12_1$) account for more than 70% of all crystalline structures consisting of single-molecule organocarbon compounds.[32] In addition, as shown in Table S1, the three reference-crystal structures are all within the scope of the statistical results, that is, each crystal has two formula units: one formula unit is treated as an asymmetric unit; and their space groups are all $P2_1$. Furthermore, the arTTF-PMDI and TTF-arPMDI crystals are assembled through favorable intermolecular interactions which are likely responsible for their relatively high polarizations. Thus, we just utilize the three reference crystals as benchmarks to filter a large number of packing structures to predict some highly promising TTF- and PMDI-based crystals with high polarizations.

Based on the reference packing structures of three new crystals, we can select a $\pi-\pi$ stacking DA pair ($MF_{\pi-\pi}$), a hydrogen bonding DA pair (MF_{HB}), and a DA pair in the $a-c$ plane with energy-favorable orientation (MF_{layer}) as the promising MFs (see Figure 2). Different from the crystal-structure search targeted for the experimental arTTF-arPMDI crystal, here both TTF-based and PMDI-based molecules are treated as independent rigid entities to generate packing structures. For the TTF-arPMDI crystal, the hydrogen bonding in its reference structure is quite special. Each arPMDI molecule acts as both a proton donor and an acceptor. One of diethylene glycol arms of the arPMDI molecule donates a proton to the carbonyl group of an adjacent arPMDI molecule in the neighboring stack, while one of its carbonyls accepts a proton in the neighboring stack. A more complex MF_{HB} is chosen for TTF-arPMDI. As shown in Figure 2, two hydrogen-bonded PMDIs are grouped as a rigid entity, and each TTF molecule is treated as a rigid entity. With the predetermined MFs, we only make use of two formula units in each crystal as the starting point. Accordingly, the space groups in the crystal search can be narrowed down to P1, P-1, or $P2_1$. During the filtering of generated packing structures, we only keep the packing structures of each new crystal whose lattice parameters are within the range $80° \leq \alpha \leq 100°$, $\beta \pm 10°$, and $80° \leq \gamma \leq 100°$ with respect to the reference crystals in each search run. After analyzing crystal similarity with respect to the reference

Table 1. Space Groups, Total Energies, Lattice Parameters, and Volumes of Unit Cells of Predicted TTF- and PMDI-Based Crystals in High- and Low-Symmetry Structures

	crystal	space group	energy (eV)	length (å)[a]			angle (deg)[a]			volume (Å)
				a	b	c	α	β	γ	
				arTTF-PMDI						
I[b]	HS[c]	$P2_1$	−563.358	4.525	12.534	17.443	90.0	111.3	90.0	921.0
	LS[c]	$P1$	−563.274	4.502	12.316	17.799	90.0	113.3	90.0	906.4
II[b]	HS	$P2_1$	−563.070	8.623	10.019	10.813	90.0	104.8	90.0	903.2
	LS	$P1$	−562.935	8.552	9.998	10.708	90.0	103.4	90.0	890.6
III[b]	HS	$P2_1$	−563.045	12.107	9.614	7.961	90.0	93.0	90.0	925.4
	LS	$P1$	−562.564	11.971	9.624	7.517	90.0	92.2	90.0	865.1
				TTF-arPMDI						
I	HS	$P2_1$	−789.280	11.043	6.846	15.467	90.0	97.5	90.0	1159.3
	LS	$P1$	−788.226	10.899	6.818	15.277	90.0	96.9	90.0	1127.0
II	HS	$P2_1$	−787.178	8.735	8.401	17.202	90.0	105.0	90.0	1219.3
	LS	$P1$	−786.784	8.386	8.563	17.299	90.0	104.8	90.0	1201.0
III	HS	$P2_1$	−787.177	6.971	14.648	11.877	90.0	88.3	90.0	1212.2
	LS	$P1$	−786.253	6.852	14.605	11.733	90.0	87.4	90.0	1173.0
				TTF-PMDI						
HS		$P2_1$	−469.773	10.963	9.444	8.400	90.0	108.0	90.0	827.1
LS		$P1$	−469.561	10.938	9.455	8.271	90.0	108.6	90.0	810.7

[a]Considering lattice parameter differences between the experimental arTTF-arPMDI crystal, DFT-optimized crystal, and crystal-search-predicted one, errors for lattice length and angle parameters in our theoretical prediction can be on the order of 0.6 Å and 1°, respectively. [b]The Roman numeral refers to different crystal types; the smaller the number is, the lower total energy (see above) the crystal has. [c]HS and LS denote high- and low-symmetry structures, respectively.

structures, about dozens of packing structures without much crystal similarity are chosen for further geometry optimization using the DFT method. The final structures and corresponding energies of the new crystals are summarized in Table S5. Last, for arTTF-PMDI and TTF-arPMDI crystals, the most stable crystals with energy difference less than 5 meV/atom are given in Table S6, and for TTF-PMDI crystal, those with energy difference less than 10 meV/atom are given in Table S6. Note that the energies of the reference arTTF-PMDI and TTF-PMDI crystals are actually not within the 5 meV/atom and 10 meV/atom energy difference. Only the energy of the reference TTF-arPMDI crystal is lower than those of generated crystals.

Finally, seven arTTF-PMDI, seven TTF-arPMDI, and four TTF-PMDI crystals are collected for possible evaluation of their ferroelectric properties. All the stable crystals contain two formula units (i.e., two MFs) (Table S6), and all belong to one of the two space groups: P-1 and P2$_1$. The crystals with P-1 space-group symmetry cannot have polarization due to inversion symmetry. Those stable crystals with the P2$_1$ space-group symmetry are summarized in Table 1 (lattice parameters) and in Table 2 (spontaneous polarizations). These packing structures are viewed as high-symmetry structures. To illustrate the structure change during the ferroelectric switching under an external electric field, low-symmetry packing structures of these crystals are also generated (see Section S3) for further investigation.

III. RESULTS AND DISCUSSION

As mentioned above, the extensive crystal search results in three stable arTTF-PMDI (numbered as I, II, and III), three stable TTF-arPMDI (also numbered as I, II, and III), and one stable TTF-PMDI crystals, all with the space group of P2$_1$ (high-symmetry structures) (see Table 1). Their corresponding low-symmetry structures are also derived from the DFT optimization while applying an electric field to the high-symmetry structure (see Section S3 for more details). The

Table 2. Total Spontaneous Polarizations (Unit: $\mu C/cm^2$) of Predicted High- and Low-Symmetry TTF- and PMDI-Based Crystals, Computed Based on DFT and Berry Phase Methods

		a	b	c
		arTTF-PMDI		
I[a]	HS[b]	0	127	0
	LS[b]	0	103	0
II[a]	HS	0	−115	0
	LS	40	−144	−29
III[a]	HS	0	−60	0
	LS	−60	−64	37
		TTF-arPMDI		
I	HS	0	27	0
	LS	22	41	−46
II	HS	0	23	0
	LS	0	23	0
III	HS	0	29	0
	LS	−15	51	−25
		TTF-PMDI		
HS		0	29	0
LS		2	−9	0

[a]The Roman numeral refers to different crystal types; the smaller the number is, the lower the free energy (see values in Table 1) the crystal has. [b]HS and LS denote high- and low-symmetry structures, respectively.

spontaneous polarizations of all the HS and LS crystals are given in Table 2. Compared to the computed polarization (25 $\mu C/cm^2$) for the experimental arTTF-arPMDI crystal, all the HS TTF- and PMDI-based crystals exhibit either comparable or significantly higher spontaneous polarizations (23−127 $\mu C/cm^2$). Especially for the three arTTF-PMDI crystals, their polarizations are remarkably high, i.e., 127 $\mu C/cm^2$ for crsytal I, −115 $\mu C/cm^2$ for II, and −60 $\mu C/cm^2$ for III. All the HS

crystals are polarized along the *b* axis. The large values of polarization stem from the ionic displacement (see Table S2(b)). To understand the origin of high polarizations and their anisotropic nature, the HS crystals (with $P2_1$ space group) and corresponding superimposed unit cells of HS (red) and LS (green) structures for each crystal are illustrated in Figures 3
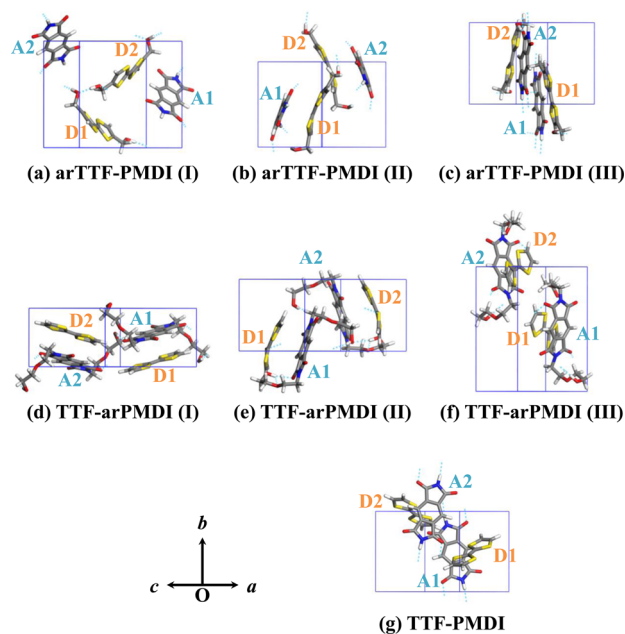

Figure 3. High-symmetry (with $P2_1$ space group) structures of predicted TTF- and PMDI-based crystals. Electron donor and acceptor molecules are denoted by D and A, respectively. The view is along the direction that bisects the *a*-O-*c* angle.

and 4, respectively. In these crystals, complex hydrogen bonds are spatially extended, resulting in tightly packed networks. From superposition of HS and LS crystals in Figure 4, no distinct site-to-site proton transfer is seen between two phases of each crystal. Therefore, the hydrogen bonds only serve as connecting bridges in TTF- and PMDI-based crystals.

In the arTTF-PMDI (**I**) crystal (Figure 3a), the electron donor (arTTF) and acceptor (PMDI) molecules do not stack in alternating fashion, and they form uniform π-stacking columns along the *a* axis. In the *b*−*c* plane, arTTF and PMDI molecules form hydrogen bonds with arTTF and PMDI molecules, respectively, in the neighboring π-stacking columns. The hydrogen bonding chain that connects arTTF molecules (e.g., D1D2D1D2) or PMDI molecules (e.g., A1A2A1A2) show a zigzag pattern in the *b*−*c* plane (Figure 3a). Upon the phase transition from HS to LS via electric-field switching (Figure 4a), the two electron donors, D1 and D2, rotate slightly around the surface normal of the TTF molecule, while the two electron acceptors, A1 and A2, slip a bit within the *b*−*c* plane. Although the phase transition appears to lose the crystal symmetry, the polarization still arises along the *b* axis (from 127 $\mu C/cm^2$ of HS to 103 $\mu C/cm^2$ of LS). Based on the computed dipole moments of arTTF and PMDI molecules (Figure 1), we know that these molecules do not possess large permanent dipole moments. Hence, the molecular dipoles alone cannot explain the magnitude or polarity of the high polarization. Within the arTTF-PMDI (**I**) crystal, molecules interact with each other via π−π interaction, charge transfer, and hydrogen bonding, among others. The high polarization along the *b* axis

may be attributed to a subtle interplay among all the weak intermolecular interactions, which can even overcome the dilute dipole density inherent to the molecular crystals.

The arTTF-PMDI (**II**) crystal (Figure 3b) is a charge-transfer complex with the mixed stack along the *a* axis. The crystal entails a complex hydrogen-bonding network. Each arTTF molecule preserves two protons of "arms" to form hydrogen bonds with carbonyl O atoms of two neighboring PMDI molecules. One ═NH group of PMDI molecule forms hydrogen bond with carbonyl O atom of the other PMDI molecule, and the other ═NH group forms hydrogen bond with hydroxyl O atom of arTTF molecule. Upon the phase transition (Figure 4b), although the motion of A1 cannot be recognized, the D1, D2, and A2 slip slightly in the *a*−*c* plane. Such a small molecular displacement induces even higher polarization along the *b* axis, and also induces high polarization about 40 $\mu C/cm^2$ and −29 $\mu C/cm^2$ along *a* and *c* axes, respectively. For the flexible "arms" and small electron donor and acceptor molecules, their motion can be easily switched under the electric field to produce high polarization.

In the arTTF-PMDI (**III**) crystal (Figure 3c), the arTTF and PMDI molecules are alternately stacked with partial π-electron overlapping between one of the five-membered rings of the TTF core and one of the five-membered rings of the PMDI core in the column along the crystallographic [101] direction. Here, arTTF molecules act as proton donors to form hydrogen bonds with carbonyl O atoms of PMDI molecules. PMDI molecules can form heteronuclear N−H···O hydrogen bonds with other PMDI molecules. In Figure 4c, the donor and acceptor molecules within the arTTF-PMDI(**III**) crystal notably slip along *a* and *c* axes when changing from HS to LS structure. The LS structure can be additionally polarized along *a* and *c* axes with values of polarization of about −60 and 37 $\mu C/cm^2$, respectively.

The TTF-arPMDI(**I**) crystal (Figure 3d) exhibits typical electron-donor−acceptor-mixed stacking columns along the *b* direction. Moreover, each arPMDI molecule acts as a proton donor and an acceptor simultaneously. One of the diethylene glycol arms of the arPMDI molecule donates a proton to the carbonyl group of the adjacent arPMDI molecule in the neighboring stack, while one of its carbonyls accepts another proton. From Figure 4d we can see that D1 and A1 molecules slip a bit along the *c* axis, and D2 and A2 slip slightly along the *a* axis during the phase transition. Accordingly, the LS crystal can be polarized along *a* and *c* axes with the polarization of about 22 and −46 $\mu C/cm^2$, respectively, which cannot be found in the HS structure.

The TTF-arPMDI(**II**) crystal (Figure 3e) has mixed stack columns along the *a* axis. The hydrogen bonds in this crystal are relatively weak. One of the "arms" of the arPMDI molecule preserves a proton to form hydrogen bonds at the same time with the ether O atom in this "arm" and the carbonyl O atom in the PMDI core, and the other "arm" supplies a proton to form a very weak hydrogen bond with the S atom of the TTF molecule. Due to the weak hydrogen-bonding network, the molecules in the crystal slip notably along *a* and *c* axes when changing from HS to LS structures (Figure 4e). The D2 molecule also slips somewhat along the *b* direction. However, the polarizations of two phases are comparable with each other both in magnitude (∼23 $\mu C/cm^2$) and in polarization direction (along the *b* axis).

The TTF-arPMDI(**III**) crystal (Figure 3f) has the charge-transfer columns along the *a* axis. Two "arms" of the arPMDI
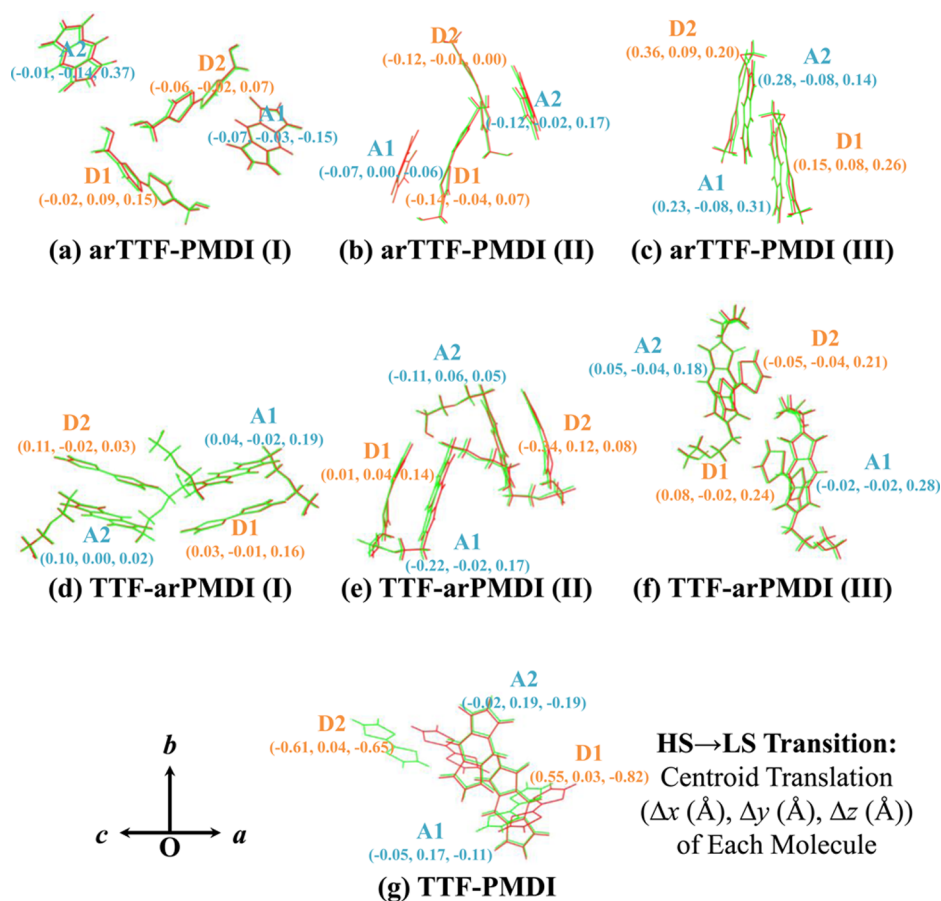
Figure 4. Illustrations of superimposed unit cells of high-symmetry (red) and low-symmetry (green) structures of TTF- and PMDI-based crystals. Electron donor and acceptor molecules denoted by D and A, respectively. Cartesian coordinates corresponding to the centroid translation from high-symmetry to low-symmetry structures (lower right panel) of the donor and acceptor molecules are also highlighted in orange and blue, respectively.

molecule interconnect with two neighboring arPMDI molecules through the homonuclear O−H···O hydrogen bonds. Upon phase transition (Figure 4f), four molecules in the crystal all slip along the c axis. The polarization along the b axis changes from 29 to 51 $\mu C/cm^2$, and the polarization along the a and c axes arises with a value of about −15 and −25 $\mu C/cm^2$, respectively.

Last, in the TTF-PMDI crystal (Figure 3g), electron donor and acceptor molecules do not have "arms". Two adjacent ═ NH groups and carbonyl O atoms of PMDI molecules play the role of proton donors and acceptors to form hydrogen bonds along the b axis with two neighboring PMDI molecules. In the unit cell, the PMDI molecules form staggered $\pi−\pi$ stacking column along the [101] direction, and two TTF molecules form a segregated uniform $\pi−\pi$ stacking column along the b axis as well. As shown in Figure 4g, upon the phase transition, the PMDI molecules exhibit relatively small slip along the b and c axes, compared to TTF molecules, due to the hydrogen bonding. The TTF molecules exhibit the largest a- and c-axis slip among all the phase transitions discussed here. Because of such a large slip for electron donor TTF molecules upon the phase transition, the polarity reversal along the b axis can be seen from 29 to −9 $\mu C/cm^2$, and the small polarization emerges along the a axis. Especially for other HS and LS crystals discussed above and even the high-symmetry TTF-PMDI crystals, their polarization arises from the ionic displacement. However, the low-symmetry TTF-PMDI crystal

has a large electronic contribution to the polarization along all three axes (see Table S2(b)).

All the newly predicted two-component (electron donor and acceptor) molecular crystals show remarkably high spontaneous polarizations (23–127 $\mu C/cm^2$). These values are either comparable to or much higher than the computed value (25 $\mu C/cm^2$) for the state-of-the-art experimental arTTF-arPMDI system. Their low-symmetry structures, switched by the electric field, are also predicted. These crystals are likely to exhibit room-temperature ferroelectricity. The high polarization may be attributed to the complicated interplay among weak intermolecular interactions such as $\pi−\pi$ stacking, charge transfer, and hydrogen bonding. The ferroelectricity of these TTF- and PMDI-based crystals stems generally from the ionic displacement. As the external stimuli change, these crystals may exhibit polarity reversal and electronic polarizations.

By and large, most of these two-component organic molecular crystals show charge-transfer characteristics with mixed-stacking π columns except arTTF-PMDI(**I**) and TTF-PMDI crystals. In the latter two crystals, electron donors or acceptors can form segregated uniform $\pi−\pi$ stacking columns. We perform additional spin-nonpolarized DFT calculations of their band structures and density of states (DOS), particularly the DOS projected onto electron-donor and -acceptor molecules of the experimental and new TTF- and PMDI-based crystal (see Figures S2−S5 of the Supporting Information). The DFT calculations suggest that both arTTF-PMDI(**I**) and TTF-PMDI crystals have nearly zero

band gaps. It appears that the highest occupied molecular orbitals (HOMOs) of two donor molecules and the lowest unoccupied molecular orbitals (LUMOs) of two acceptor molecules hybridize and give rise to two bonding and antibonding bands near the Fermi level. For other charge-transfer crystals, their two bonding and antibonding bands near the Fermi level are mostly contributed by the HOMOs of TTF-based donors and the LUMOs of PMDI-based acceptors, respectively. The much weaker hybridization between HOMOs of donors and LUMOs of acceptors opens up the band gap. Note in passing that the NI transition of TTF-CA and TTF-BA crystals requires a narrow charge gap which may lead to electric leakage and degrade the spontaneous polarization.[4,11] Thus, for TTF- and PMDI-based crystals, if the crystals entail charge-transfer and hydrogen bonding interactions at the same time, it would be beneficial to their ferroelectric performance.

IV. CONCLUSION

Inspired by recent successful synthesis of arTTF-arPMDI crystal with room-temperature ferroelectricity,[18] three new ferroelectric co-crystals are designed by removing the short hydroxymethyl arm and/or the long diethylene glycol "arm" from the arTTF and arPMDI molecules. To predict low-energy packing structures for the tailored designed arTTF-PMDI, TTF-arPMDI, and TTF-PMDI crystals, a newly developed computational approach that combines polymorph predictor with DFT geometry relaxation is employed for screening effective crystal structure. Surprisingly, a number of newly predicted crystals possess high to ultrahigh spontaneous polarizations ($23-127$ μC/cm^2), all having the space group of $P2_1$. All the crystals are polarized along the b axis and their high polarizations arise from the ionic displacement. The high polarizations may be attributed to collective contributions of all the weak intermolecular interactions (e.g., $\pi-\pi$ stacking, charge transfer, and hydrogen bonding) to overcome their nonpolarity of constituent electron donor and acceptor molecules. Based on an electric-filed-switched surface model, the low-symmetry structures of the new TTF- and PMDI-based crystals are also derived. By comparing the high-symmetry with low-symmetry structures of crystals, we find that the electric polarization can be very sensitive to atomic positions. A small molecular displacement can bring high polarizations along a and c axes and even induce polarity reversal and electronic contribution to polarization. Note also that one of our goals for the computer-aided design of organic ferroelectric complexes is to address the question that which packing structures are more likely to give rise to room-temperature ferroelectricity. Our extensive search of the TTF- and PMDI-based crystals suggests that the hydrogen-bonded charge-transfer complexes with flexible and small-sized electron donor and acceptor molecules can be promising candidates to possess ultrahigh polarization. We propose that the space groups of synthesized crystals from these precursors can serve as a handy indicator for judging possible high/low polarizations. Of course, confirmation of the predicted packing structures and their high or ultrahigh polarization must await future experiments.

ASSOCIATED CONTENT

Ⓢ Supporting Information

More computational details are presented in Sections S1−S3. Computed properties of the reference and newly designed crystals, including detailed lattice parameters, high- and low-symmetry structures, and spontaneous polarizations are given

in Tables S1 and S2 and Figure S1; the COMPASS force field parameters and calibration of force field are shown in Tables S3 and S4; detailed packing structures generated from the crystal search are shown in Tables S5 and S6; computed band structures and DOS projected onto donor and acceptor molecules are displayed in Figures S2−S5. This material is available free of charge via the Internet at http://pubs.acs.org.

AUTHOR INFORMATION

Corresponding Author
*E-mail: xzeng1@unl.edu

Notes
The authors declare no competing financial interest.

REFERENCES

(1) Dawber, M.; Rabe, K. M.; Scott, J. F. *Rev. Mod. Phys.* **2005**, *77*, 1083.
(2) Scott, J. F. *Science* **2007**, *315*, 954.
(3) Valasek, J. *Phys. Rev.* **1921**, *17*, 475.
(4) Horiuchi, S.; Tokura, Y. *Nat. Mater.* **2008**, *7*, 357.
(5) Goldsmith, G. J.; White, J. G. *J. Chem. Phys.* **1959**, *31*, 1175.
(6) Noda, K.; Ishida, K.; Kubono, A.; Horiuchi, T.; Yamada, H.; Matsushige, K. *J. Appl. Phys.* **2003**, *93*, 2866.
(7) Poulsen, M.; Ducharme, S. *IEEE Trans. Dielectr. Electr. Insul.* **2010**, *17*, 1028.
(8) Horiuchi, S.; Kumai, R.; Okimoto, Y.; Tokura, Y. *Chem. Phys.* **2006**, *325*, 78.
(9) Kagawa, F.; Horiuchi, S.; Tokunaga, M.; Fujioka, J.; Tokura, Y. *Nat. Phys.* **2010**, *6*, 169.
(10) Kobayashi, K.; Horiuchi, S.; Kumai, R.; Kagawa, F.; Murakami, Y.; Tokura, Y. *Phys. Rev. Lett.* **2012**, *108*, 237601.
(11) Horiuchi, S.; Hasegawa, T.; Tokura, Y. *J. Phys. Soc. Jpn.* **2006**, *75*, 051016.
(12) Horiuchi, S.; Ishii, F.; Kumai, R.; Okimoto, Y.; Tachibana, H.; Nagaosa, N.; Tokura, Y. *Nat. Mater.* **2005**, *4*, 163.
(13) Horiuchi, S.; Kumai, R.; Tokura, Y. *J. Am. Chem. Soc.* **2005**, *127*, 5010.
(14) Horiuchi, S.; Kumai, R.; Tokura, Y. *Chem. Commun.* **2007**, 2321.
(15) Horiuchi, S.; Tokunaga, Y.; Giovannetti, G.; Picozzi, S.; Itoh, H.; Shimano, R.; Kumai, R.; Tokura, Y. *Nature* **2010**, *463*, 789.
(16) Horiuchi, S.; Kumai, R.; Tokura, Y. *Adv. Mater.* **2011**, *23*, 2098.
(17) Horiuchi, S.; Kagawa, F.; Hatahara, K.; Kobayashi, K.; Kumai, R.; Murakami, Y.; Tokura, Y. *Nat. Commun.* **2012**, *3*, 1308.
(18) Tayi, A. S.; Shveyd, A. K.; Sue, A. C.-H.; Szarko, J. M.; Rolczynski, B. S.; Cao, D.; Kennedy, T. J.; Sarjeant, A. A.; Stern, C. L.; Paxton, W. F.; Wu, W.; Dey, S. K.; Fahrenbach, A. C.; Guest, J. R.; Mohseni, H.; Chen, L. X.; L.Wang, K.; Stoddart, J. F.; Stupp, S. I. *Nature* **2012**, *488*, 485.
(19) Frisch, M. J.; Trucks, G. W.; Schlegel, H. B.; Scuseria, G. E.; Robb, M. A.; Cheeseman, J. R.; Scalmani, G.; Barone, V.; Mennucci, B.; Petersson, G. A.; Nakatsuji, H.; Caricato, M.; Li, X.; Hratchian, H. P.; Izmaylov, A. F.; Bloino, J.; Zheng, G.; Sonnenberg, J. L.; Hada, M.; Ehara, M.; Toyota, K.; Fukuda, R.; Hasegawa, J.; Ishida, M.; Nakajima, T.; Honda, Y.; Kitao, O.; Nakai, H.; Vreven, T.; Montgomery, J. A.; Peralta, J. E.; Ogliaro, F.; Bearpark, M.; Heyd, J. J.; Brothers, E.; Kudin, K. N.; Staroverov, V. N.; Kobayashi, R.; Normand, J.; Raghavachari, K.; Rendell, A.; Burant, J. C.; Iyengar, S. S.; Tomasi, J.; Cossi, M.; Rega, N.; Millam, J. M.; Klene, M.; Knox, J. E.; Cross, J. B.; Bakken, V.;

6435

dx.doi.org/10.1021/ja5017393 | *J. Am. Chem. Soc.* 2014, 136, 6428−6436

Adamo, C.; Jaramillo, J.; Gomperts, R.; Stratmann, R. E.; Yazyev, O.; Austin, A. J.; Cammi, R.; Pomelli, C.; Ochterski, J. W.; Martin, R. L.; Morokuma, K.; Zakrzewski, V. G.; Voth, G. A.; Salvador, P.; Dannenberg, J. J.; Dapprich, S.; Daniels, A. D.; Farkas, O.; Foresman, J. B.; Ortiz, J. V.; Cioslowski, J.; Fox, D. J. *Gaussian 09*, revision A.02; Gaussian, Inc.: Wallingford, CT, 2009.

(20) *Materials Studio*, v 6.1; Accelrys Inc.: San Diego, CA, 2012.

(21) Kresse, G.; Furthmüller, J. *Comput. Mater. Sci.* **1996**, *6*, 15.

(22) Kresse, G.; Furthmüller, J. *Phys. Rev. B* **1996**, *54*, 11169.

(23) King-Smith, R. D.; Vanderbilt, D. *Phys. Rev. B* **1993**, *47*, 1651.

(24) Vanderbilt, D.; King-Smith, R. D. *Phys. Rev. B* **1993**, *48*, 4442.

(25) Resta, R. *Rev. Mod. Phys.* **1994**, *66*, 899.

(26) Rigby, D.; Sun, H.; Eichinger, B. E. *Polym. Int.* **1997**, *44*, 311.

(27) Sun, H.; Ren, P.; Fried, J. R. *Comput. Theor. Polym. Sci.* **1998**, *8*, 229.

(28) Sun, H. *J. Phys. Chem. B* **1998**, *102*, 7338.

(29) Boys, S. F.; Bernardi, F. *Mol. Phys.* **1970**, *19*, 553.

(30) Simon, S. l.; Duran, M.; Dannenberg, J. J. *J. Chem. Phys.* **1996**, *105*, 11024.

(31) Karasawa, N.; W, A. G., III *J. Phys. Chem.* **1989**, *93*, 7320.

(32) Baur, W. H.; Kassner, D. *Acta Crystallogr., Sect. B* **1992**, *48*, 356.